STATIC SCENE STATISTICAL NON-UNIFORMITY CORRECTION

THESIS

Adrian M. Catarius, First Lieutenant, USAF

AFIT-ENG-MS-15-M-062

DEPARTMENT OF THE AIR FORCE
AIR UNIVERSITY

AIR FORCE INSTITUTE OF TECHNOLOGY

Wright-Patterson Air Force Base, Ohio

AFIT-ENG-MS-15-M-062

STATIC SCENE STATISTICAL NON-UNIFORMITY CORRECTION

THESIS

Presented to the Faculty

Department of Electrical and Computer Engineering

Graduate School of Engineering and Management

Air Force Institute of Technology

Air University

Air Education and Training Command

in Partial Fulfillment of the Requirements for the

Degree of Master of Science in Electrical Engineering

Adrian M. Catarius, B.S.E.E.

First Lieutenant, USAF

March 2015

AFIT-ENG-MS-15-M-062

STATIC SCENE STATISTICAL NON-UNIFORMITY CORRECTION

Adrian M. Catarius, B.S.E.E.
First Lieutenant, USAF

Committee:

Maj Michael D. Seal (Chairman)

Stephen C. Cain, PhD (Member)

Mark E. Oxley, PhD (Member)

AFIT-ENG-MS-15-M-062

Abstract

Non-Uniformity Correction (NUC) is required to normalize imaging detector Focal-Plane Array (FPA) outputs due to differences in the end-to-end photoelectric responses between pixels. Currently, multi-point NUC methods require static, uniform target scenes of a known intensity for calibration. Conversely, scene-based NUC methods do not require a priori knowledge of the target but the target scene must be dynamic. The new Static Scene Statistical Non-Uniformity Correction (S3NUC) algorithm was developed to address an application gap left by current NUC methods. S3NUC requires the use of two data sets of a static scene at different mean intensities but does not require a priori knowledge of the target. The S3NUC algorithm exploits the random noise in output data utilizing higher order statistical moments to extract and correct fixed pattern, systematic errors. The algorithm was tested in simulation and with measured data and the results indicate that the S3NUC algorithm is an accurate method of applying NUC. The algorithm was also able to track global array response changes over time in simulated and measured data. The results show that the variation tracking algorithm can be used to predict global changes in systems with known variation issues.

Acknowledgments

I would like to express my gratitude to my research advisor, Major Michael Seal, for not only imparting his wisdom and experience throughout my research, but also for sharing the pain, providing general good humor, and always letting me know when pertinent information belonged in my copy-book. A special thanks go out to my committee members, Dr. Stephen Cain and Dr. Mark Oxley, for providing guidance, resources, and for checking the voluminous amount of derivation. I must also thank Lieutenant Colonel Brian Neff for providing code and data early on. Finally, I want to thank my fellow officers both within and outside my section that often provided an outlet to share the mutual frustration in the interest of preserving my sanity during our stay here.

Adrian M. Catarius

Table of Contents

Page

List of Figures

List of Tables

List of Acronyms

Acronym	Definition
ADC	Analog-to-Digital Converter
APD	Avalanche Photodiode
ASC	Advanced Scientific Concepts
AWGN	Additive White Gaussian Noise
CCD	Charge-Coupled Device
CMOS	Complementary Metal-Oxide-Semiconductor
FOV	Field of View
FPA	Focal-Plane Array
GPU	Graphics Processing Unit
LADAR	Laser Detection and Ranging
LSE	Log-Squared Error
NUC	Non-Uniformity Correction
RMSE	Root Mean Squared Error
RSD	Relative Standard Deviation
S3NUC	Static Scene Statistical Non-Uniformity Correction

STATIC SCENE STATISTICAL NON-UNIFORMITY CORRECTION

I. Introduction

All photodetector arrays suffer from systematic and random noise. On the array, there are systematic deviations in the microfabrication of the individual detectors. Deviations in physical dimensions and material properties lead to deviations in the gain and bias between detectors. The gain and bias deviations between each detector introduce a fixed, systematic noise pattern on the output data. Photodetector arrays also suffer from random noise in the detection and digitalization process that can be characterized using random processes. While random noise can be mitigated with a filter on the output, fixed pattern systematic noise requires a separate calibration process for removal.

Extracting and correcting the fixed pattern of gain and bias deviations is called Non-Uniformity Correction (NUC). Currently there are two common methods of performing NUC. The two-point method uses data from two calibrated targets of a uniform and known intensity. The gain and bias corrections produced via the two-point method may introduce and preserve radiometric calibration. The primary drawback to this method is the requirement for the uniform targets of known intensity, which are difficult to produce. The other common NUC methods are scene-based corrections, which does not require calibrated targets. The drawback to scene-based NUC methods is that they require dynamic data sets that are either long enough to average to a constant value or a priori knowledge of how the scene is moving.

A new method of NUC was derived to garner the benefits of producing radiometrically accurate gain and bias corrections without the need for known calibration sources. Static Scene Statistical Non-Uniformity Correction (S3NUC) utilizes higher order statistical

moments to exploit the random noise in the output to extract and correct for the systematic noise. The noise sources fit within a linear model of a photodetector for which the moments are calculated. The derived moments of this linear model produce a system of equations that may be solved for radiometrically unskewed values for the gain and bias of the detector.

The new method of S3NUC was derived to address down-array, pixel-to-pixel deviations, similar to current NUC methods. Using the same equations applied in a cross-array configuration, the algorithm can track global variation in an array's gain and bias. The S3NUC and variation tracking algorithms were tested in simulation and with real data. The results produced indicate that S3NUC can produce accurate gain and bias corrections without the need for a priori knowledge of the target source.

II. Background

2.1 Introduction

In a typical camera system, an image is created from photons collected at an aperture and focused onto a photodetector Focal-Plane Array (FPA) [4, 5]. The FPA converts incident photons into electrons that are then digitized by an Analog-to-Digital Converter (ADC). Systematic noise is introduced from deviations in the gain and bias of the FPA and any system amplifiers [17]. The random arrival of photons at a photodector is known to follow a Poisson random process [5]. Random noise is also introduced in the collection and digitization processes and the noise follows well defined probability distributions. The random noise is commonly removed using filters or averaging. To remove the systematic deviations from a photodetection system, one of two NUC methods are commonly employed. Additionally, gain and bias can change over time which creates operational problems in some systems, particularly Laser Detection and Ranging (LADAR) systems.

2.2 Digital Camera Model

2.2.1 Optics.

All the cameras used in the research conducted had at least one lens collecting photons at the aperture. The lenses enable the aperture to be much larger to collect more photons from the incident field without requiring a large detector area [4]. A larger aperture also allows the optical system to have a smaller minimum resolvable distance. Two objects closer together angularly than the minimum distance will be indistinguishable from a single, larger object. The minimum resolvable angular distance in radians, θ, is calculated from the aperture diameter in meters, D, and the wavelength of light, λ, using

$$\theta = 1.220\frac{\lambda}{D}. \tag{2.1}$$

Thus a larger aperture diameter will produce fields with smaller resolvable angular distance and have a greater degree of resolution [4]. The minimum resolvable distance also dictates the spacing between elements on an array needed to fully sample the field produced by the optics. In general, photodetector arrays are designed to meet the resolvable distance to fully sample the intensity field but some systems do not meet the requirements and spatially under-sample the field [4].

2.2.2 Photodetector Arrays.

Photodetector arrays are comprised of many individual photodetectors, or pixels, typically arranged in a rectangular array defined as a FPA. There are many different types of photodetectors available for different operating wavelengths and applications. The three cameras used in the research conducted have arrays made up of Complementary Metal-Oxide-Semiconductor (CMOS), Charge-Coupled Device (CCD), and Avalanche Photodiode (APD) sensors. Both CMOS and CCD sensors are comprised of a single p-n junction photodiode [31]. The photodiode is operated with a reverse bias to produce a depletion region in the junction. Photons incident on the depletion region free electron-hole pairs which travel through the diode generating a current that is collected into an electrical charge. The electrical charge is transferred by logic gates to the digitization circuit. The difference between CMOS and CCD sensors is the specific configuration of logic gates used to transfer the charge level on the p-n junction [12]. CMOS arrays typically have additional circuitry within the FPA compared to CCD arrays. The additional circuitry can be used to suppress fixed pattern noise [12].

APD sensors are similar in operation to CMOS sensors but can achieve a higher gain ratio of photons collected to electrons produced [14]. Fundamentally, the APD is a diode with a higher reverse bias applied to drive it into the avalanche breakdown mode. The

higher gain allows APD sensors to produce images from lower intensity incident fields. This saturates the depletion region with election-hole pairs [28]. As the electron-hole pair are freed and begin to move, the strong reverse bias accelerates the carriers to the point where they have enough kinetic energy to excite more carriers. The quantity of electrons excited by a single photon is defined as the APD gain and is dependent on both the physical parameters of the device and the amount of reverse bias across the junction [14].

FPAs can have from a few thousand individual photodetectors to many millions. With large arrays of detectors, manufacturing each individual detector to be identical to the others becomes a difficult process. Deviations in physical dimensions and material properties lead to deviations in the gain and bias of the detectors [17, 21, 23].

2.2.3 Analong-to-Digital Conversion.

The ADC in a camera is responsible for converting the collected charge from the photodetector into a digital or discrete value. The conversion quantizes the analog charge input into a discretely sampled output. The sampling process introduces an amount of quantization error that is a function of the precision of the ADC used [7]. The error takes the form of systematic noise in the output signal as the error is a function of the input signal value [17].

2.3 Random and Systematic Noise

2.3.1 Photon Shot Noise.

Most types of photodetectors collect photons for a fixed period of time to generate a measurable charge level. Over that period of time, the detector collects and stores the charge from all arriving photons. Photon arrivals are mathematically represented as impulse functions [4]. The mathematical operation of the detector collecting the photons is integrating over the impulses for the fixed period of time, called the integration time of the sensor. As the integration time grows longer for a detector collecting from a constant

source, the average amount of charge per period increases resulting in a higher output. The same relationship exists for shorter integration times resulting in lower outputs.

A significant source of noise in any photodetector system output is the effects of photon shot noise [2, 11, 22]. Shot noise is a result of the Poisson process that characterizes how photons arrive at a photo detector [5]. The Poisson process is used for characterizing a series of impulses arriving at random time intervals apart. Over a fixed time period, there will be an expected number of impulse arrivals. The rate at which the impulses arrive is defined as $\lambda(t)$ and the mean value of impulses to arrive between the two times t_1 and t_2 is defined to be $\bar{\lambda}$ and is calculated using

$$\bar{\lambda} = \int_{t_1}^{t_2} \lambda(t)dt. \tag{2.2}$$

Given $\bar{\lambda} \in \mathbb{R}$, the probability that $K \in \mathbb{N}$ impulses arrive during the time interval, $P(K, t_1, t_2)$, is defined by a Poisson distribution [5] which has a density function in the form

$$P(K, t_1, t_2) = \frac{\left(\int_{t_1}^{t_2} \lambda(t)\,dt\right)^K}{K!} exp\left(-\int_{t_1}^{t_2} \lambda(t)\,dt\right) = \frac{\bar{\lambda}^K}{K!} e^{-\bar{\lambda}}. \tag{2.3}$$

Assuming that photons behave like particles in this case and that their arrival in a time interval is statistically independent from the photons arriving in a different, non-overlapping interval, then the Poisson process can define photon arrivals at a photodetector during an integration time. The random nature of the arrival times can distort images collected with photodetectors. For an object with a constant mean photon emission, $\bar{K}$ will be a constant but the output value of the camera will vary randomly according to probability density function defined in (2.3).

2.3.2 Clock Noise.

Clock drift and jitter are both errors in the clock signal that, in cameras, defines the integration times [12, 32]. Clock drift, also called wander, is defined as a slow trend of change in the clock frequency. The slow change can add up to an increasing deviation from

the specified clock frequency and the actual frequency. In a general camera operation, drift will slowly change the integration time of the detector. If a camera images a constant source and if the drift slowly increases the integration time, the output images will slowly get brighter. The same relationship applies to the reverse situation.

Clock jitter is defined as a fast change in clock frequency [32]. The threshold between drift and jitter is defined to be changes occurring at $10Hz$. Where drift is often systematic and has a clear trend, jitter is usually random. Jitter is quantified by calculating the difference between the measured period of the clock per cycle and the ideal, fixed period between cycles. The effects of jitter become more prevalent as clock frequency increases[1]. The effects of jitter on a camera appear similar to photon shot noise in that the output is fluctuating randomly around a mean value as the integration times change randomly. In that aspect, clock jitter is treated as an additive source of random noise.

2.3.3 Other Sources of Random Noise.

There are other sources of noise that affect the output of any camera system. One such source is thermal noise that is produced by any detector that is not at absolute zero ($0K$) [22]. The noise is a product of diffusion current that is generated by p-n junction above $0K$ [29]. The thermal noise affects the charge collected by the photodetector prior to conversion to digital values and is an additive source of noise. Thermal noise can be reduced, but not eliminated, by actively cooling the photodetector.

Some but not all random sources of noise in camera systems have well defined probability distributions. For the purposes of the research conducted, all random sources of noise aside from photon shot noise are assumed to be additive in the final output data. The assumption is based on the fact that sources such as thermal and clock jitter noise are additive sources [1, 3]. Grouping together many random variables allows the application of the central limit theorem. With many random variables with finite means and variances, the distribution of the sum of the random variables approaches a Gaussian, or Normal,

distribution [5]. Applying the central limit theorem to the random noise sources in a camera allows the assumption that the sum of all non-Poisson noise produces Additive White Gaussian Noise (AWGN) in the final output data.

2.4 Current Non-Uniformity Correction Methods

As indicated in Section 2.2.2, FPAs will have detectors with different responses due to deviations in the manufacturing process. The nonuniform gain and bias values over the individual detectors will result in a fixed pattern imposed on the output data [17, 21, 23]. The fixed pattern cannot be differentiated from the target scene and is undesirable in most applications. Additionally, the random noise complicates the process of extracting and correcting for the pattern. Techniques for NUC have been created for extracting the fixed pattern and compensating for the random noise to correct the output data.

2.4.1 Multi-Point NUC.

One widely used method of NUC is collecting data with an array of a perfectly uniform photon source [21]. One-point correction utilizes the fact that if the source is uniform, any fixed pattern seen at the output is due to gain and bias deviations in the array. If the intensity of the photon source is known, the fixed pattern can be further solved for a direct radiometric relation from photons to digital output value. The one-point method was further improved to a two-point method using two uniform sources of different and known intensities. In both methods, the random noise is averaged out before correction to remove its effects. The two-point method has been experimentally verified for many types of sensors and has become a standard technique for NUC [8]. In some FPAs, the response over different intensities can be nonlinear, necessitating a multi-point NUC to accurately correct the output [25].

2.4.2 Scene-Based NUC.

Another subset of NUC methods use scene-based information extract the fixed pattern. One method relies on the concept of constant statistics [10, 18]. Constant statistics assumes

that a single pixel's response over time will have a constant mean and standard deviation. From the mean and standard deviation, the fixed pattern noise is extracted and used to correct the output data. For the constant statistics assumptions to be valid, the scene being imaged cannot be stationary for too long within the data set [10]. The averaging required to compute the mean and standard deviation has the additional effect of removing the random noise present in the data.

A different scene-based method of NUC utilizes global motion tracking between frames in a data sequence [8, 11]. If an object with a constant intensity is being imaged and is being optically shifted to all detectors on the array, then the detectors have all been subject to the same intensity at some point in the data stream. The raw data is first filtered to remove the effects of random noise [11]. Then, combining the data stream across the objects movement effectively creates a uniform reference to use to extract the fixed pattern.

2.5 Variation Over Time

Variation in the gain and bias of an FPA over time can be a result of external conditions, such as temperature, or a result of systematic errors in the system [9]. In cameras, the variation over time can continuously produce systematic noise that will not be corrected by a one-time NUC. In some applications, such as LADAR, the variation over time produces additional effects beyond systematic noise [28].

One particular system being used in the research conducted is an Advanced Scientific Concepts (ASC) "TigerEye" 3D Flash LADAR system. LADAR systems have additional operational characteristics beyond that of a photodetector camera. In the basic operation of a Flash LADAR, a pulse of laser light is sent towards the target [22]. The pulse reflects off of the target and returns to the LADAR's aperture. A measurement of the time from the laser pulse emission to its return to the array is used to calculate the range from the LADAR to the target. Using the TigerEye's 128×128 APD array, each pixel can produce an independent range measurement to build a three-dimensional image [13, 15, 30].

One of the possible sources of error in the TigerEye system is from the transient response of the voltage regulator supplying power to the APD array. On a previous, developmental version of the APD array, each pixel had a dark current demand of 14.4 *nA*. Across all 16384 pixels, the array has a combined dark current demand of 0.238 *mA* [28]. If the array were to receive a 4.7 *nJ* return pulse from a laser, assuming the APD array has a constant gain of 10 and that 52% of the energy will be contained in 5 samples, the current demand of the array will increase to 984 *mA*. This gain by a factor of 4169 over the dark current will translate to the voltage regulator having to compensate for the demand in an extremely short time frame of 5 *ns*. In the current version of the Tigereye, the voltage regulator and APD specifications are neither identified nor able to be removed for testing. However, it is assumed that the APD array behaves in a very similar fashion and the voltage regulator cannot provide such a short transient response.

In a previous experiment conducted with the developmental version of the APD array, a halogen lamp with a hemispheric reflector was used to provide a near-constant stream of photons to each pixel in the APD array. The LADAR was run without the laser timing system on and range-samples were collected for fifty-four overlapping ranges. Another prior experiment had showed that the APD array is biased at initial activation rather than the start of collection for each range-sample. The property allowed the overlapping range-samples to have a significant factor of overlap [28]. The overlap enabled a concatenation of the sets of data to show a long term trend in the recorded data as seen in Figure 2.1. There is a significant amount of short-term variation that shows an almost periodic and sinusoidal trend. On a long-term trend, the values slowly drop in a behavior similar to an exponential function [28].

The previous work attributed the main cause of the variation to the voltage regulator circuit and its transient response. Variation in the amount of voltage bias applied to the APD array will result in a variation in the gain of the array and will result in a noisy data trend

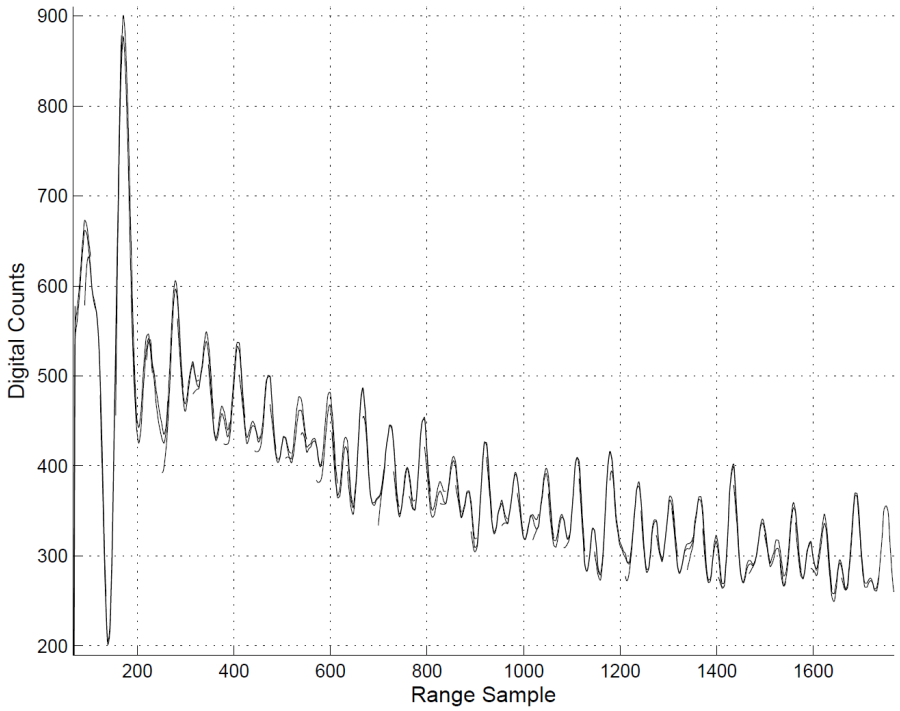

Figure 2.1: Overlay of Illuminated Conditioned Responses for Fifty-Four Ranges, Used with Permission [28]

compared to the expected constant trend. Additionally, the type of variation above would contribute to ranging error in that an object of some distance away would be measured to be farther than it actually was from the LADAR [16, 28].

2.6 Constraints to Current Non-Uniformity Correction Methods

The primary drawback to one and two-point NUC methods is the requirement for uniform sources of known intensities [11, 21]. The equipment required includes a source as well as any additional optics, mirrors, and electronics. The cost of the equipment is generally high and the complexity of the setup typically restricts the method to laboratory settings [8]. Scene-based NUC methods generally do not require any additional equipment. However, without knowing the exact intensity of the scene or object being imaged, scene-based methods cannot preserve the radiometric accuracy of the conversion of photons to digital values for the detector. For some applications, radiometric calibration is required.

Therefore, an ideal NUC method would provide radiometric accuracy preserving gain and bias corrections without the need for a priori knowledge of the target scene. Additionally, the current NUC methods may not be applicable to a pulse LADAR system due to the way they operate.

III. Methodology

3.1 Introduction

The fundamental principle of S3NUC is that is utilizes the error produced by the random noise to correct the systematic errors in the system. The newly derived S3NUC method relies on a linear photodetection and digitization model previously defined by Hayal *et al* [11]. The model uses the sum of two statistical distributions, a Poisson distribution for the photon arrival and a Gaussian distribution for other sources of noise. First, second, and third order central moments of the model distribution can be analytically derived. Using two sets of data at different photo-intensities, the moments produce a complete linear system of equations for calculating the gain, bias, photocounts, and noise variance of the photodetector.

Other current NUC methods either do not use a statistics based approach [24, 26, 27] or only use the first and second order moments in their algorithm [10, 18]. Furthermore, most methods require a filter or averaging to remove random noise in the FPA output before addressing the systematic noise. The S3NUC algorithm instead exploits the random noise using statistical models to solve for the systematic noise present in the output.

Two different implementations of the algorithm were implemented. The first implementation extracts the fixed pattern noise from a FPA. This implementation was evaluated with simulated data and then applied to data collected from CMOS and CCD based cameras. The second implementation tracks the variation trends in both the mean gain and bias of the FPA over time. This variation tracking implementation was also evaluated with simulation data, then applied to CMOS and CCD camera data. In addition to the camera tests, it was applied to a LADAR system which was known to exhibit gain variation over its ranging interval.

3.2 Terminology

To maintain a consistent use of terminology, certain terms are defined as follows. Each image in a data set is referred to as a frame. Each frame is comprised of many pixels with each pixel corresponding to the output from a single photodetector in the FPA. In the TigerEye LADAR data, a "cube" of frames refers to twenty frames taken consecutively and starting after a defined period of time after the laser pulse was emitted. In the LADAR data collected, consecutive cubes of frames all start after the same period from the laser pulse. A "down-array" implementation, or S3NUC, refers to taking the moments of a vector of data points for a single pixel location on the array. The moments are used to calculate gain and bias estimates to correct images. A "cross-array" implementation, or variation tracking implementation, refers to taking the moments of all the data points in a single frame. The results of variation tracking are the mean gain and bias values for the whole FPA over time. The expectation of a random variable is represented as $E[\cdot]$. Statistical means are denoted with the bar above the variable, such as $\bar{A}$ being the mean of the random variable A. The variance is represented as σ^2 with a subscript to define which variable it is the variance of, such as σ_A^2 for the random variable A. Similarly, the skewness of a variable is represented as γ with a subscript, such as γ_A for the random variable A.

3.3 S3NUC Derivation

The following linear model is used for a photodetector. The digital output value, D, which is a single digital value from one pixel that is a function of the gain of the system, G, multiplied by the photocount incident to the pixel, K, plus the bias, B, and a zero-mean AWGN term, n. The AWGN is assumed to be zero-mean as any non-zero mean is indistinguishable from the bias value, B. The AWGN represents the accumulations from all electronic noise after the detector, such as the ADC, and n is assumed to be independent of K. The equation for the resulting model is

$$D = GK + B + n. \tag{3.1}$$

Each pixel's digital value, D, is assumed to be independent from all other pixels on the array. The gain, G, is also assumed to be a constant value, corresponding to a linear photoresponse.

For the sake of clarity, all derivations are made for a single pixel. In implementation, the calculations are extended in parallel to all pixels in the array. To implement NUC on an array, it is necessary to solve for the gain, bias, and the variance of the AWGN. The photocount is target scene dependent and is assumed to follow a Poisson process model [5]. To generate a set of well posed equations, the first, second, and third order statistical moments are required.

3.3.1 Derivation of the First Moment.

The first order moment, or mean, of the data is defined as $\bar{D}$ and is calculated by taking the expectation of Equation (3.1)

$$\bar{D} = E[D] = E[GK + B + n]. \tag{3.2}$$

The photodetection process model is a linear combination of two random variables and two deterministic values. The expected value of a deterministic variable is itself. The expectation calculation is a linear operation and can be reduced to

$$\bar{D} = GE[K] + B + E[n]. \tag{3.3}$$

The mean of the AWGN is assumed to be zero and the mean of the photocount, $\bar{K}$ is unknown but deterministic. Substituting these values into Equation (3.3), the mean of the data reduces to

$$\bar{D} = G\bar{K} + B. \tag{3.4}$$

Equation (3.4) is the first of the equations required for a complete system used in S3NUC.

3.3.2 Derivation of the Second Moment.

A second equation is generated from the second order central moment, or variance, of the data. The variance of the data, σ_D^2, is calculated from expectation of the square of the

data mean subtracted from the data

$$\sigma_D^2 = E[(D - \bar{D})^2]. \tag{3.5}$$

Equations (3.1) and (3.4) are substituted into Equation (3.5) to produce

$$\sigma_D^2 = E[(GK + B + n - (G\bar{K} + B))^2]. \tag{3.6}$$

The bias terms are cancelled out and Equation (3.6) reduces to

$$\sigma_D^2 = E[(GK + n - G\bar{K})^2]. \tag{3.7}$$

The polynomial inside the expectation operation is expanded to produce

$$\sigma_D^2 = E[G^2\bar{K}^2 - 2G^2\bar{K}K + G^2K^2 - 2G\bar{K}n + 2GKn + n^2]. \tag{3.8}$$

All of the deterministic terms can be pulled out of the expectation and Equation (3.8) reduces to

$$\sigma_D^2 = G^2\bar{K}^2 - 2G^2\bar{K}E[K] + G^2E[K^2] - 2G\bar{K}E[n] + 2GE[Kn] + E[n^2]. \tag{3.9}$$

Employing the mean value of the AWGN, zero, and the photocount mean further reduces Equation (3.9) to

$$\sigma_D^2 = G^2\bar{K}^2 - 2G^2\bar{K}^2 + G^2E[K^2] + 2GE[Kn] + E[n^2]. \tag{3.10}$$

In Equation (3.10), three expectation operations remain. The first, $E[K^2]$ is the second order moment about the origin of a Poisson random variable and is defined to be [6]

$$E[K^2] = \bar{K}^2 + \bar{K}. \tag{3.11}$$

The second expectation, $E[Kn]$, is the joint expectation of K and n. The random variables are assumed to be independent, so the joint expectation reduces to

$$E[Kn] = E[K]E[n]. \tag{3.12}$$

The final remaining expectation from Equation (3.10) is $E[n^2]$, which is a second order moment about the origin of a Gaussian distribution and is defined to be [19]

$$E[n^2] = \sigma_n^2 + E[n]^2. \tag{3.13}$$

In Equation (3.13), the noise variance, σ_n^2 is an unknown constant. Substituting Equations (3.11), (3.12), and (3.13) into Equation (3.10) produces

$$\sigma_D^2 = G^2\bar{K^2} - 2G^2\bar{K}^2 + G^2(\bar{K^2} + \bar{K}) + 2GE[K]E[n] + \sigma_n^2 + E[n]^2. \tag{3.14}$$

The AWGN mean, $E[n] = 0$, so two terms drop out in Equation (3.14) and the expression in parentheses expands to

$$\sigma_D^2 = G^2\bar{K^2} - 2G^2\bar{K^2} + G^2\bar{K^2} + G^2\bar{K} + \sigma_n^2. \tag{3.15}$$

The three terms in Equation (3.15) with $\bar{K^2}$ cancel and the variance of the data is reduced to

$$\sigma_D^2 = G^2\bar{K} + \sigma_n^2. \tag{3.16}$$

Equation (3.16) is the second equation required for the S3NUC system.

3.3.3 Derivation of the Third Moment.

The third order central moment, skewness, is used to generate the third equation. The skewness of the data, γ_D, is defined to be expectation of the cube of the data mean subtracted from the data and divided by the standard deviation of the data, σ_D,

$$\gamma_D = E\left[\left(\frac{D - \bar{D}}{\sigma_D}\right)^3\right] \tag{3.17}$$

The standard deviation of the data is a known, deterministic value and can be removed from the expectation operation to produce

$$\gamma_D = \frac{1}{\sigma_D^3}E[(D - \bar{D})^3]. \tag{3.18}$$

Equations (3.1) and (3.4) are substituted into Equation (3.18) to produce

$$\gamma_D = \frac{1}{\sigma_D^3} E[(GK + B + n - (G\bar{K} + B))^3]. \tag{3.19}$$

The bias terms cancel out and Equation (3.18) reduces to

$$\gamma_D = \frac{1}{\sigma_D^3} E[(GK + n - G\bar{K})^3]. \tag{3.20}$$

The polynomial inside the expectation operation is expanded to yield

$$\gamma_D = \frac{1}{\sigma_D^3} E[G^3(-\bar{K}^3) + 3G^3\bar{K}^2K - 3G^3\bar{K}K^2 + G^3K^3 + 3G^2\bar{K}^2n - 6G^2\bar{K}Kn + 3G^2K^2n - 3G\bar{K}n^2 + 3GKn^2 + n^3]. \tag{3.21}$$

Once again, the deterministic values can be pulled outside the expectation operation and all joint expectations can be split similarly to Equation (3.12) to produce

$$\gamma_D = \frac{1}{\sigma_D^3}(G^3(-\bar{K}^3) + 3G^3\bar{K}^2E[K] - 3G^3\bar{K}E[K^2] + G^3E[K^3] + 3G^2\bar{K}^2E[n] - 6G^2\bar{K}E[K]E[n] + 3G^2E[K^2]E[n] - 3G\bar{K}E[n^2] + 3GE[K]E[n^2] + E[n^3]). \tag{3.22}$$

All AWGN means are zero as a nonzero mean would be indeterminate from the bias, so the equation reduces to

$$\gamma_D = \frac{1}{\sigma_D^3}(G^3(-\bar{K}^3) + 3G^3\bar{K}^2E[K] - 3G^3\bar{K}E[K^2] + G^3E[K^3] - 3G\bar{K}E[n^2] + 3GE[K]E[n^2] + E[n^3]). \tag{3.23}$$

The photocount mean has been defined as $\bar{K}$ and is substituted in along with Equations (3.11) and (3.13) yielding

$$\gamma_D = \frac{1}{\sigma_D^3}(G^3(-\bar{K}^3) + 3G^3\bar{K}^3 - 3G^3\bar{K}(\bar{K}^2 + \bar{K}) + G^3E[K^3] - 3G\bar{K}\sigma_n^2 + 3G\bar{K}\sigma_n^2 + E[n^3]). \tag{3.24}$$

In Equation (3.24), there are two unknown expectations, $E[K^3]$ and $E[n^3]$. For K, a Poisson random variable, the third order moment about the origin is determined to be [6]

$$E[K^3] = \bar{K}^3 + 3\bar{K}^2 + \bar{K}. \tag{3.25}$$

The third order moment about the mean for a Gaussian random variable, such as n, is determined to be [19]

$$E[n^3] = 3E[n]\sigma_n^2 + E[n]^3. \tag{3.26}$$

Substituting Equations (3.25) and (3.26) into Equation (3.24) produces

$$\begin{aligned}\gamma_D = \frac{1}{\sigma_D^3}(G^3(-\bar{K}^3) + 3G^3\bar{K}^3 - 3G^3\bar{K}(\bar{K}^2 + \bar{K}) + G^3(\bar{K}^3 + 3\bar{K}^2 + \bar{K}) \\ -3G\bar{K}\sigma_n^2 + 3G\bar{K}\sigma_n^2 + 3E[n]\sigma_n^2 + E[n]^3).\end{aligned} \tag{3.27}$$

The zero mean of the AWGN terms and the expressions in parentheses are expanded to produce

$$\begin{aligned}\gamma_D = \frac{1}{\sigma_D^3}(-G^3\bar{K}^3 + 3G^3\bar{K}^3 - 3G^3\bar{K}^3 - 3G^3\bar{K}^2 + G^3\bar{K}^3 + 3G^3\bar{K}^2 \\ +G^3\bar{K} - 3G\bar{K}\sigma_n^2 + 3G\bar{K}\sigma_n^2).\end{aligned} \tag{3.28}$$

All similar expressions are combined and several terms cancel out to reduce the equation to

$$\gamma_D = \frac{G^3\bar{K}}{\sigma_D^3}. \tag{3.29}$$

Equation (3.29) along with Equations (3.4) and (3.16) form the basis for the S3NUC system of equations. The system of equations is shown in Table 3.1. To solve for all of the unknown quantities, $G, B, \bar{K}, \sigma_n^2$, two data sets with different intensities are required, generating a complete system of six equations in five unknowns.

Table 3.1: S3NUC System of Equations

Moment Equation
$\bar{D} = G\bar{K} + B$
$\sigma_D^2 = G^2\bar{K} + \sigma_n^2$
$\gamma_D = \frac{G^3\bar{K}}{\sigma_D^3}$

3.3.4 Derivation of the Fourth Moment.

In the model in Equation (3.1), there are four unknowns, $G, B, \bar{K}, \sigma_n^2$, in three equations. To produce the fourth equation, a fourth moment, excess kurtosis, may also be derived. However, during simulation, the method requires excessively large data sets to produce precise enough results to be useful. Tens of millions of frames of data were required. The reason large data sets are required comes from the small value of the excess kurtosis and the comparatively large standard deviation in the estimates of the excess kurtosis.

The equation for the excess kurtosis, $\mathcal{K}_D$, of the model in Equation (3.1) was derived to be

$$\mathcal{K}_D = \frac{G^4 \bar{K}}{\sigma_D^4}. \tag{3.30}$$

Using the excess kurtosis equation with the equations in Table 3.1, there are four unknown variables and four equations in the system. In practice, the excess kurtosis is small, a few hundredths in value. However, with a finite set of data points, the excess kurtosis is an estimate of the actual amount of excess kurtosis and has a degree of uncertainty. Data was simulated according to the model in Equation (3.1) for increasing sample sizes. At data sets in excess of 100,000 samples in size, the standard deviation of the excess kurtosis calculated from the data was significantly large compared to the excess kurtosis value. This translated to gain estimates with a low degree of precision to the point where the algorithm could not produce consistent estimates using the same starting values. Results from data sets with 10^7 samples improved performance but at that size, the algorithm is no longer practical. Therefore, the method of using a single data set and the excess kurtosis equation from Equation (3.30) was not tested further.

3.4 Method of Serial Calculation of Moments

The direct method of computing moments for a finite set of data is to load all the data points into memory and use a summation formula. For S3NUC, the amount of data

required, especially for cameras with a large number of pixels, can exceed the memory available on most computers. To alleviate the memory burden of loading all of the required frames simultaneously, the moments are computed via a serial algorithm described by Dr. Terriberry [33]. The algorithm is based on calculating the moments of a set X by splitting it into two partitions, X^A and X^B. For this algorithm, the partition A is defined as all the samples that have arrived prior to the current time and the set B is a single, new sample. As the partition B is only one value, it's mean is the same value as itself, and all higher order central moments have a value of zero. N is defined as the total sample size of A and B combined, N^B is the sample size of B and has a value of 1 and thus, the size of A, noted as N^A in the original equations [33], has a size of $N - 1$. Substituting these values into Dr. Terriberry's equations produces a set of update formulas for computing the three moments needed for S3NUC. In Equations 3.31-3.35, X^B is the incoming sample from the set X, and all variables with a with a prime notation are values for the next iteration [33].

$$N = N + 1, \tag{3.31}$$

$$\delta = X^B - \mu, \tag{3.32}$$

$$\mu' = \mu + \frac{\delta}{N}, \tag{3.33}$$

$$M_3' = M_3 + \delta^3 \frac{(N-1)(N-2)}{N^2} - 3\frac{M_2\delta}{N}, \tag{3.34}$$

$$M_2' = M_2 + \delta^2 \frac{(N-1)}{N}. \tag{3.35}$$

The implementation of this method begins with N, μ, M_2, and M_3 all set to zero. Equations 3.31-3.35 are looped through and at the conclusion of each iteration, μ', M_2', and M_3' update to μ, M_2, and M_3 respectively for the next iteration. At the conclusion of the loop, the mean of the set X, μ_X, the variance, σ_X^2, and the kurtosis, γ_X can be calculated

using

$$\mu_X = \mu, \tag{3.36}$$

$$\sigma_X^2 = \frac{M_2}{N}, \tag{3.37}$$

$$\gamma_X = \frac{\sqrt{N} M_3}{M_2^{\frac{3}{2}}}. \tag{3.38}$$

The serial method reduces the computations per iteration down to simple arithmetic that is readily computed in parallel using Graphics Processing Unit (GPU)s. The algorithm loads a single frame of data and a set of sums for each pixel are calculated in parallel using Equations 3.32-3.35. The next frame replaces the previous frame in memory and the set of sums are updated until all of the frames have been processed. The resultant set of sums is then used to calculate the moments for each pixel in the data set using Equations 3.36-3.38. This same method can be extended to arbitrary order moments [20].

3.5 System Solution

The S3NUC system of equations in Table 3.1 has three equations and four unknowns. To generate another set of equations, two data sets of different photo-intensities are used. The second set of data adds one new unknown value but supplies three more equations. With five unknowns and six equations, the system is over-determined and the unknowns can be solved. The first data set, D_1, is used as the reference and is defined to have a total mean photocount, $\bar{K}_{D_1 Tot}$, of a mean value $\bar{K}$

$$\bar{K}_{D_1 Tot} = \bar{K}. \tag{3.39}$$

The second data set, D_2, has a different mean photocount due to the difference in intensities between data sets. The mean difference in photocounts is defined as $\Delta\bar{K}$. If D_1 is the darker of the two data sets, $\Delta\bar{K}$ will be positive. If D_2 is darker, $\Delta\bar{K}$ will be a negative value. The sum of multiple Poisson random variables is also Poisson [6] and the total mean

photocount for D_2, $\bar{K}_{D_2Tot}$ is the sum of the mean reference and the mean difference

$$\bar{K}_{D_2Tot} = \bar{K} + \Delta\bar{K}. \tag{3.40}$$

Substituting the photocounts into the original model from Equation (3.1) yields models for both sets of data

$$D_1 = G(K) + B + n, \tag{3.41}$$

$$D_2 = G(K + \Delta K) + B + n. \tag{3.42}$$

Using Equations (3.39) and (3.40) in conjunction with the mean, variance, and skewness formulae from Equations (3.4), (3.16), and (3.29), closed form expressions for the moments for both data sets can be generated. For D_1, the mean, $\bar{D}_1$, variance, $\sigma^2_{D_1}$, and skewness, γ_{D_1}, equations are

$$\bar{D}_1 = G\bar{K} + B, \tag{3.43}$$

$$\sigma^2_{D_1} = G^2\bar{K} + \sigma^2_n, \tag{3.44}$$

$$\gamma_{D_1} = \frac{G^3\bar{K}}{\sigma^3_{D_1}}. \tag{3.45}$$

Similarly, the mean, $\bar{D}_2$, variance, $\sigma^2_{D_2}$, and skewness, γ_{D_2}, equations for D_2 are

$$\bar{D}_2 = G\bar{K} + G\Delta\bar{K} + B, \tag{3.46}$$

$$\sigma^2_{D_2} = G^2\bar{K} + G^2\Delta\bar{K} + \sigma^2_n, \tag{3.47}$$

$$\gamma_{D_2} = \frac{G^3\bar{K} + G^3\Delta\bar{K}}{\sigma^3_{D_2}}. \tag{3.48}$$

The system of equations, with two data sets, has five unknowns, G, B, $\bar{K}$, $\Delta\bar{K}$, and σ^2_n, so it is over-determined. An over-determined system will produce multiple sets of solutions for the unknown variables. In this system, $\bar{K}$, B, and σ^2_n each have two solutions that are produced. The gain, G, it is equal to the difference between the two variances in Equations (3.44) and (3.47) divided by the difference between the two means

in Equations (3.43) and (3.46)

$$G = \frac{\sigma_{D_2}^2 - \sigma_{D_1}^2}{\bar{D}_2 - \bar{D}_1}. \tag{3.49}$$

With the gain determined, the mean photocount difference, $\Delta\bar{K}$, can be solved for from the difference in the means in Equations (3.43) and (3.46) divided by the determined gain from Equation (3.49)

$$\Delta\bar{K} = \frac{\bar{D}_2 - \bar{D}_1}{G}. \tag{3.50}$$

Using the determined gain, the mean reference photocount, $\bar{K}$, can be calculated from the product of the skewness and standard deviation from D_1 cubed divided by the gain cubed

$$\bar{K} = \frac{\gamma_{D_1}\sigma_{D_1}^3}{G^3}. \tag{3.51}$$

The bias, B, can be calculated from the product of the determined values of the gain and mean photocount, subtracted from $\bar{D}_1$

$$B = \bar{D}_1 - G\bar{K}. \tag{3.52}$$

Finally, the noise variance, σ_n^2, is calculated from the product of the determined gain squared and the photocount count subtracted from the data variance from D_1

$$\sigma_n^2 = \sigma_{D_1}^2 - G^2\bar{K}. \tag{3.53}$$

Because the system is over-determined, for $\bar{K}$, B, and σ_n^2, there are alternative solutions available using calculations from the second set of data. The three alternative equations are

$$\bar{K} = \frac{\gamma_{D_2}\sigma_{D_2}^3 - G^3\Delta\bar{K}}{G^3}, \tag{3.54}$$

$$B = \bar{D}_2 - G\bar{K} - G\Delta\bar{K}, \tag{3.55}$$

$$\sigma_n^2 = \sigma_{D_2}^2 - G^2\bar{K} - G^2\Delta\bar{K}. \tag{3.56}$$

Equations (3.54), (3.55), and (3.56) will theoretically produce the same values as Equations (3.51), (3.52), and (3.53) but in practice the results will be less precise. In

practice, the values for the unknowns will be estimates of the true values with an amount of error between the estimate and the true value. Equations (3.54), (3.55), and (3.56) require the use of the estimate for $\Delta\bar{K}$ which introduces error not present in Equations (3.51), (3.52), and (3.53). The error results in less accurate estimates produced for $\bar{K}$, B, and σ_n^2 and therefore, Equations (3.54), (3.55), and (3.56) are not used in S3NUC.

The derivation of the S3NUC system of equations may be implemented to examine gain and bias deviations in imaging array data for two different purposes. The first implementation, the down-array analysis, produces estimates of the individual gain and bias values for each pixel in the array. To implement, many frames of data must be collected for both data sets. The scenes being imaged do not need to be uniform but they should change as little as possible to achieve an accurate statistical estimate. For each data set, the vector of values being used are from one pixel from all frames of data. Applying the S3NUC equations to the pixel's vector of values will provide a gain and bias estimate for that particular pixel. The application can be repeated for all pixels in the array to estimate gain and bias values for every pixel. These estimates may be used to correct the nonuniform, fixed pattern noise present in the output data. This implementation, including the correction, is referred to as S3NUC.

The second implementation, the cross-array analysis, produces estimates of the average gain and bias values across the array for a pair of frames. In a pair of frames, the target scene is identical with different photo intensities. The data points used to calculate the moments are all of the pixels across each frame. Moments of the frames are used in the S3NUC system of equations to solve for the average gain and bias values for the pair of frames. If multiple pairs of frames are collected sequentially in time and analyzed in order, the gain and bias values can be tracked over time. In systems where the gain and bias are known to vary over time, the trend of variation can be used to correct the output data. This implementation is referred to as the variation tracking algorithm.

IV. Results

4.1 Introduction

The first step to verifying the application of the S3NUC equations was to examine the trade space between precision, accuracy and sample size. Two simulations were conducted to test the precision and accuracy of the gain and bias estimates over a range of sample sizes. The number of samples required to achieve qualitatively good estimates were not prohibitively large for many applications. To verify the S3NUC equations could be used to apply NUC, a down-array analysis was performed over multiple sets of simulated data and the estimates were used to correct the image. The same analysis was applied to data collected with a CCD camera. The S3NUC equations were also tested in a cross-array analysis to verify variation tracking performance. The equations were tested with simulated data over a variety of different combinations of trends and the method was able to produce accurate trend estimates compared to the truth. Variation tracking was also applied to CMOS camera, CCD camera, and LADAR data. The results agreed with previous research in the area.

4.2 S3NUC Testing

4.2.1 Simulation Testing.

Before testing with measured data, a series of simulated tests were conducted using MATLAB. To test the precision of the estimates provided by the S3NUC method, two sets of data were generated according to Equations (3.41) and (3.42). Each data sample was generated from a mean photocount, $\bar{K}$, using a Poisson random number generator function. For the second set of data, a $\Delta\bar{K}$ constant value, equal to half the value of $\bar{K}$, was added before the random number generation operation. The AWGN was generated using a Gaussian random number generator with a specified variance. The simulation was run over

1000 independent data sets. For each set, the equations in Table 3.1 were used to estimate the gain and bias. The mean gain and bias estimates were computed from the estimates from the 1000 data sets to assess the average accuracy of the S3NUC method. Additionally, the standard deviation of the 1000 estimates was calculated to assess the precision of the estimates.

The simulation ran across 100 different data set sizes, spaced on a logarithmic scale from 1 to 100,000. The estimation was repeated over three values of $\bar{K}$, 10, 100, and 1000 to asses the effects of a changing photocount on the estimates. According to the Poisson model, a higher mean photocount equates to a higher variance in the actual photocount values which does affect some of the estimates. Futhermore, a fourth simulation was conducted including an 8-bit ADC quantization of the generated data prior to the computing the moments. The simulation with the ADC had a $\bar{K}$ value of 100.

For the gain estimates, mean estimates are plotted over the increasing sample size using the Log-Squared Error (LSE) of the mean estimates shown in Figure 4.1(a). The three tests without the ADC show a similarly decreasing trend in error over increasing sample size. The data set with the ADC shows that it reaches a much lower error value compared to the other data sets at most sample sizes. However, past a sample size of 10^4, the LSE value plateaus at a value of approximately -4.3 indicating that the quantization of the ADC limits the accuracy of the gain estimate.

The standard deviations of the gain estimates were plotted using Relative Standard Deviation (RSD) which normalizes the standard deviation, σ, to the mean estimated value, μ using the equation $RSD = \frac{\sigma}{\mu} \times 100$. The RSD plot of the gain estimates is shown in Figure 4.1(b). The RSD plot shows that after a sample size of approximately 10, the different photocount values and the inclusion of the ADC do not affect the precision of the gain estimate. The lack of change is a result of the way the photocount is divided out in Equation (3.49). This eliminates the extra variance from higher mean photocounts.

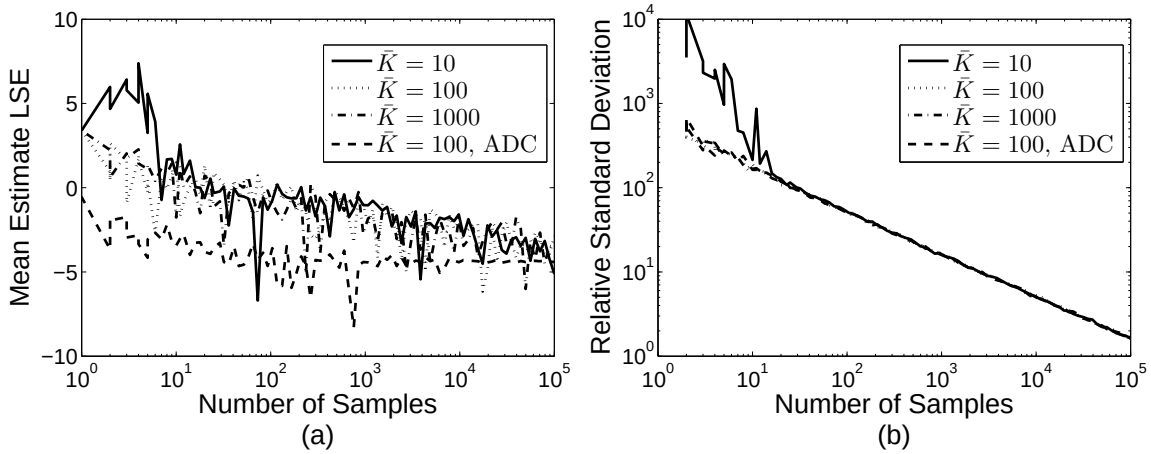

Figure 4.1: shows the Log Squared Error plot of the mean gain estimates in (a) and the Relative Standard Deviation of the estimates in (b).

The same analysis which was applied to the gain estimates was also applied to the bias estimates. The LSE plot of the mean bias estimates in Figure 4.2(a) shows that differing mean photocount values do affect the bias estimate. The lower values for $\bar{K}$ produced more accurate bias estimates across nearly all sample sizes greater than approximately 100. The data set with the 8-bit ADC showed a trend similar to the gain estimates in that it produced a more accurate estimate early on but the error stopped decreasing after a sample size of approximately 10^4. The RSD plot of the bias estimates in Figure 4.2(b) shows a similar trend in that the data sets with lower $\bar{K}$ values producing more precise estimates. The set where $\bar{K} = 1000$ does not show a clearly decreasing trend. This indicates that in situations with high photocounts, S3NUC may not be able to produce reliable estimates of the bias. This is due to the way the photocount is additive relative to the bias in Equation (3.1). Being additive, the additional variance that comes with a higher mean photocount cannot be eliminated in the same way that it is from the gain estimate. Additionally, the addition of the ADC further reduced the bias RSD for situations with the same mean photocount. The reduced RSD is due to the quantization of the ADC, which restricts the bias to within the resolution of the ADC and thus reduces the variance. However, the resolution of the

ADC limits the accuracy of the bias estimate, especially if the bias value falls in-between ADC quantization bins.

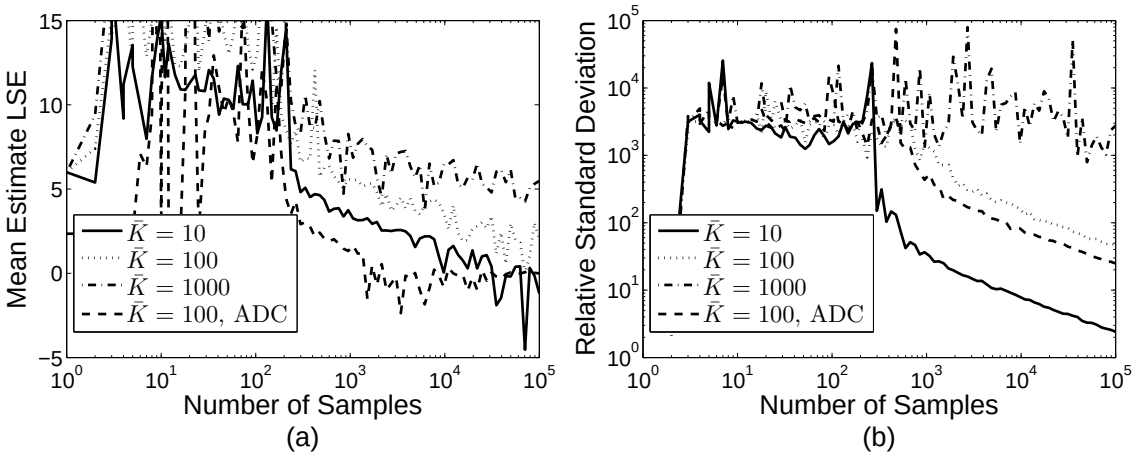

Figure 4.2: shows the Log Squared Error of the mean bias estimates in (a) and the Relative Standard Deviation of the estimates in (b).

For the gain and bias precision, the ratio of $\frac{\Delta\bar{K}}{K}$ stayed at a value of 0.5 for all four cases. To test the effects of a changing ratio, the simulation was repeated with a constant $\bar{K}$ value of 100 and four different $\Delta\bar{K}$ values of 25, 50, 100 and 200. The same RSD plots were generated for the gain and bias estimates and the results are shown in Figure 4.3. The gain RSD plot in Figure 4.3(a) shows the precision is affected by the ratio of $\frac{\Delta\bar{K}}{K}$ with a higher value resulting in a lower amount of RSD and better estimate precision. The bias RSD plot in Figure 4.3(b) shows that the precision improves much quicker when $\frac{\Delta\bar{K}}{K}$ is larger. At data sets greater than 10^4 in size, the bias estimate precision is not significantly affected by the changing ratio. For both the gain and bias estimates, the LSE trends were examined and both the gain and bias showed no change in accuracy for different ratios of $\frac{\Delta\bar{K}}{K}$.

The S3NUC method was applied in a down-array configuration to simulate NUC estimation on two pairs of simulated data sets. The first pair simulated an ideal, uniform source field. The data sets each had 20,000 128×128 pixel images. The length of the data

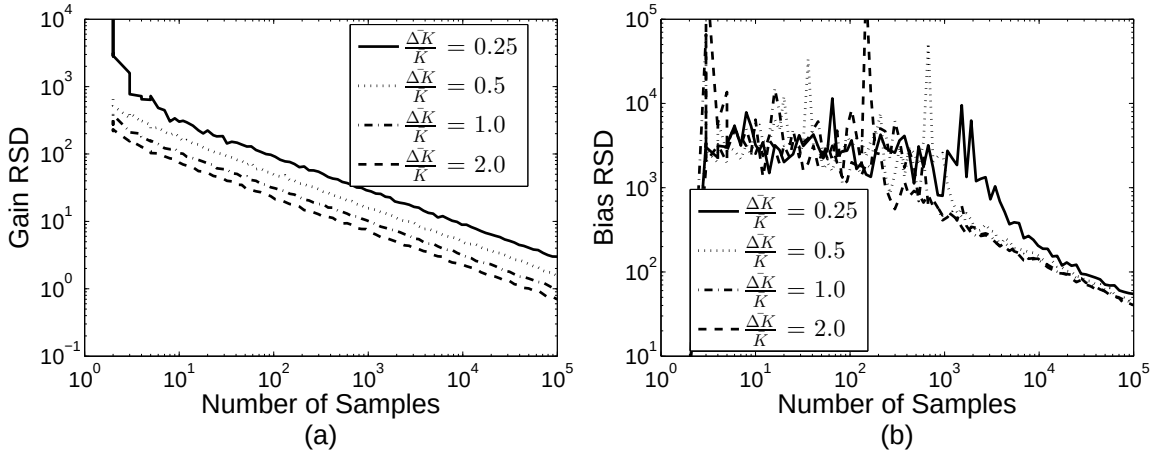

Figure 4.3: shows the Relative Standard Deviation of the gain estimates in (a) and the bias estimates in (b) over different ratios of $\frac{\Delta\bar{K}}{K}$.

sets of 20,000 was chosen to drive the precision for the gain below single digits and for the bias, below triple digits according to Figures 4.1 and 4.2. A gain screen was generated, comprised of a checkerboard of different gain values with a minimum value of 50 and a maximum of 100. The photocount matrices were generated using the same Poisson number generator from the previous simulated data.

Each matrix of generated photocounts was multiplied by the true gain matrix, summed with the bias value and the matrix of generated noise values. The process was repeated for each frame in each data set. With each data set, the mean, variance, and skewness were calculated along the set of 20,000 frames for each individual location. Once all necessary moments were calculated, Equations (3.49)-(3.53) were used to estimate the original gain, bias, photocount, and noise variance values. The true values for the bias, mean photocounts and noise variance used in this simulation are listed in Table 4.1.

After running the simulation, the fixed pattern estimate provided by the S3NUC equations was compared to the original gain pattern. The Root Mean Squared Error (RMSE) of the estimates were 1.6783 counts off from the true values. The two dimensional

Table 4.1: Values for Simulation

Parameter name	Value
B	1000
$\bar{K}$	25
$\Delta\bar{K}$	25
σ_n^2	1

correlation coefficient between the estimates and the truth was 0.9971, indicating that the gain estimate's shape was a good match to the true pattern or screen.

To verify that the S3NUC method does not require a uniform source field to produce accurate results, the same simulation was repeated with a non-uniform mean photocount. The non-uniform source field was implemented with a 128×128 pixel image that was normalized to have the same mean photocount of 25 as the previous uniform source. All other parameters, including the gain screen remained exactly the same as the previous simulation run.

The S3NUC method produced an estimate of the gain pattern that was compared to the true gain pattern. The RMSE of the estimate was 1.7195 counts off of the truth and the correlation coefficient was 0.9969. The results show that with a non-uniform source, the S3NUC method was able to produce an accurate estimate of the gain pattern. The precision did suffer compared to the uniform source field, but not significantly so. The LSE images of the gain estimates to the true gain pattern are shown in Figure 4.4 with the results from the uniform data set in (a) and the nonuniform set in (b). There are some visible signs of the original source image, or ghosting, that is affecting the accuracy of the estimates from the nonuniform data set. In the nonuniform source simulation, $\Delta\bar{K}$ is constant and $\bar{K}$ is changing over the image, giving different ratios of $\frac{\Delta\bar{K}}{\bar{K}}$ and thus different degrees of

precision over the image. The changing precision manifests itself as the ghosting seen in Figure 4.4(b).

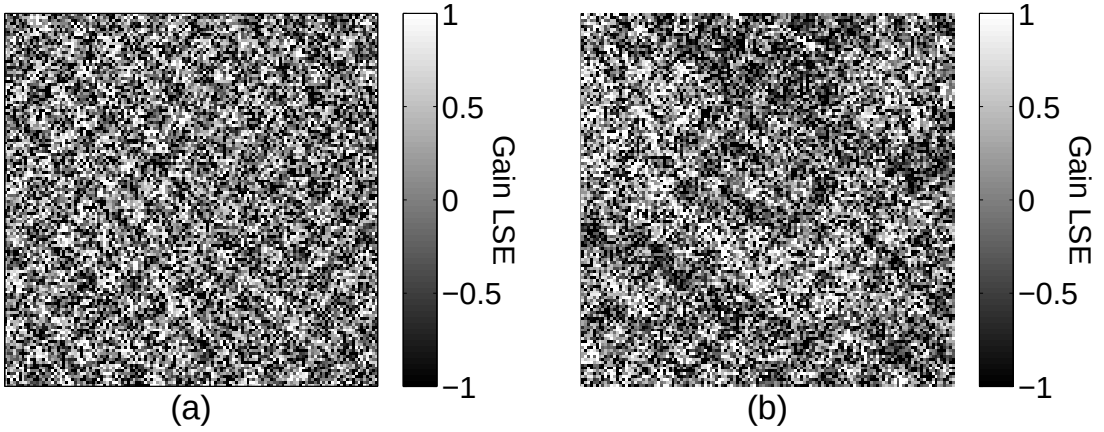

Figure 4.4: shows the LSE images of the gain estimates to the true gain pattern. The image in (a) is the LSE image of the gain estimate from the data set with the uniform source field and (b) is the LSE image from the nonuniform data set. While there is some residual checkerboard pattern in these images, it should be noted that the amount of error is very small.

To further examine the method's performance, the bias estimates from both the uniform and nonuniform data were compared. The RMSE for the uniform case was 204.1847 and the nonuniform case was 260.0308. Figure 4.5 shows the LSE images of the bias estimates to the true bias value. The results from the uniform data are in Figure 4.5(a) and from the non-uniform data are in Figure 4.5(b). Examining the results, the estimates from the non-uniform data in Figure 4.5(b) have visible signs of ghosting in the LSE image. The presence of ghosting matches with the prediction that a changing photocount will affect the precision and accuracy of the bias estimate as shown in Figure 4.2.

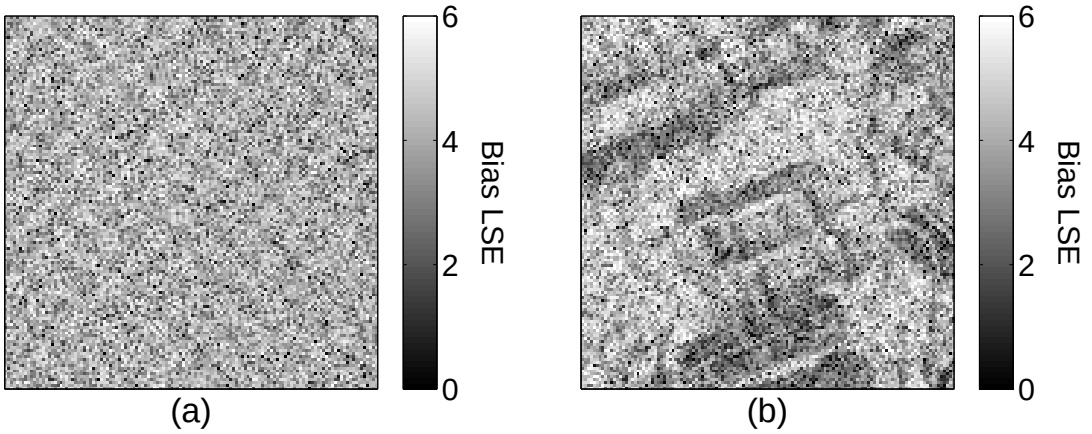

Figure 4.5: shows the LSE images of the bias estimates to the true bias value. The image in (a) is the LSE image of the bias estimate from the data set with the uniform source field and (b) is the LSE image from the nonuniform data set. Ghosting is present due to the bias estimate being affected by the changing mean photocount as shown in Figure 4.2

To complete the S3NUC process, 100 frames from the nonuniform data set was corrected using the estimated gain and bias values from the uniform data set. The mean value of the corrected images had a range from 25.0183 to 25.2312 . The 100 frames were averaged and the resultant image shows no discernable signs of the gain pattern. The averaged image had a mean of 25.1321, close in value to the original mean of 25. The RMSE of the average image with the original nonuniform source field was 3.1342. Both the single corrected frame and the averaged image show random noise because S3NUC does not perform any filtering on the noisy input images. Figure 4.6 shows an uncorrected frame in (a), a single corrected frame in (b), and the average image of 100 corrected frames in (c). Both the corrected frame and the average corrected image show that S3NUC is capable of removing fixed pattern noise in FPA read-out data using a static scene as a calibration source.

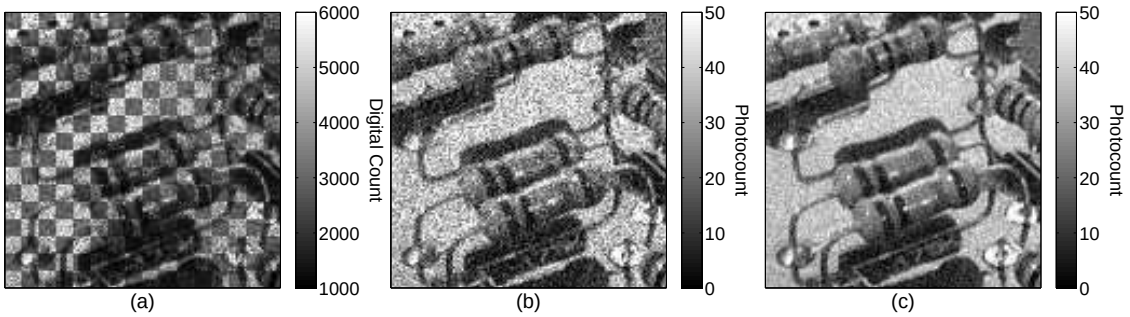

Figure 4.6: displays an uncorrected frame from the nonuniform data set in (a), a single frame S3NUC corrected using the results from the uniform data set in (b), and the average of 100 S3NUC corrected frames in (c).

The corrected frames were also used to measure the amount of remaining noise after S3NUC. With the 100 frames, each frame had the previous frame subtracted from it. The 99 difference frames were reshaped into a vector of values with a mean of -6.231×10^{-5}. The mean is close in value to zero which corresponds to the zero mean AWGN. The standard deviation of the vector of values was 7.0769, larger than the value of 1 used to generate the AWGN. This indicates that S3NUC removes systematic noise by exploiting random noise, with a side effect of adding some random error.

4.2.2 CCD Camera Results.

Several data sets were collected with a CCD camera in the same fashion as the CMOS data to test the S3NUC approach. The data collected were of an illuminated wall. The different intensities were achieved by adjusting the lens iris to vary the light being passed onto the array. 10,000 images, each 640×480 pixels large, were taken for each data set. The frames were processed with the same algorithm described in Section 3.4. Figure 4.7 shows the gain estimates in (a) and the bias estimates in (b).

The standard deviation of the gain values was 0.1774 compared to the mean gain value of 3.160. Similarly, the bias standard deviation was 6.777 compared to the mean value of 9.407. With the CCD data sets, the standard deviations were smaller than the mean

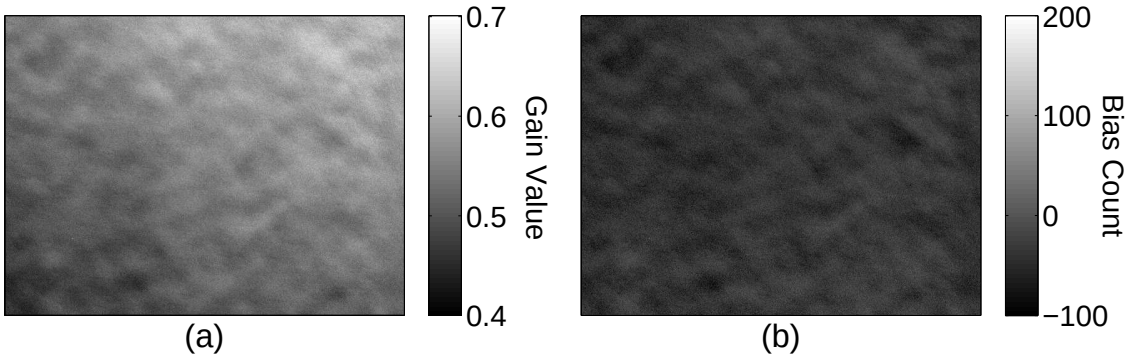

Figure 4.7: shows the gain pattern estimate from 10,000 CCD images in (a), and bias pattern estimate in (b)

value indicating an acceptable degree of precision. Both gain and bias estimates exhibit a pattern of the top right corner having higher values and the bottom left having lower values compared to the rest of the estimates. The probable cause is non-uniform lighting being exacerbated by the long data sets. Additionally, there are signs of ghosting in the gain and bias estimates. This ghosting is from the different ratios of $\frac{\Delta\bar{K}}{\bar{K}}$ caused by the constant $\Delta\bar{K}$ from the lens aperture changing and the non-uniform $\bar{K}$ from the illuminated wall. However, the pattern exhibited in the estimates is gradual and near uniform in value. Based on that fact, the camera was suspected of having NUC applied to it during manufacturing.

To verify that hypothesis, the integration time of the camera was increased to over 60 seconds to draw out any systematic noise. The resultant image shown in Figure 4.8 was clear enough to show three solvent evaporative spots left over from the FPA manufacturing. The ability to see the spots indicates that some form of NUC was previously applied to the camera and thus, no systematic noise was observed. With that knowledge, an application of S3NUC could be used for checking the performance of NUC in manufacturing.

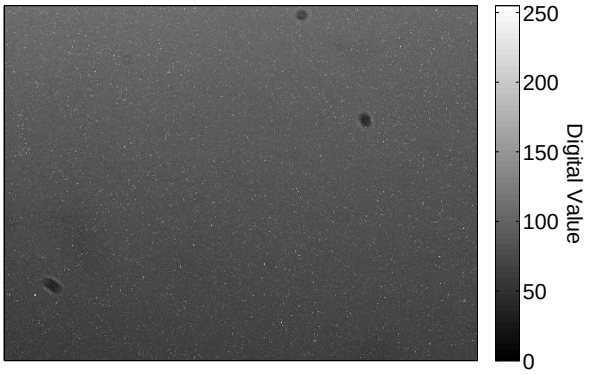

Figure 4.8: shows an image taken by the CCD camera with an integration time of 67.1 seconds. The image does not have any visual signs of fixed pattern noise. Instead, the image is clear enough to see three dark spots from solvent evaporation left over from manufacturing.

4.3 Variation Tracking Testing

4.3.1 Simulation Testing.

To examine the ability of the algorithm to track gain and bias variation, a cross-array variation tracking implementation was applied to simulated data. Each frame of data is 128 pixels square, for 16384 pixels total. With this many data points, the variance plot in Figure 4.1 indicates the results of the gain estimates should have less than one unit of variance. Two sets of data were created adhering to the model in Equation (3.1) with 100 frames in both data sets. In this simulation, the gain and bias values were varied by frame rather than held at a constant values. Each frame had the same gain and bias across the array and the values changed frame to frame. Specific gain and bias vectors were created to test different variation types. Both sets of data for each trial used the same gain and bias vectors.

In a cross-array configuration, the mean, variance, and skewness values were calculated from all the pixel values in a single frame. The moment values in one frame

from the first set of data was combined with the moments from the matching frame in the second set of data in the S3NUC equations to produce gain and bias estimates for the entire simulated array. The process was repeated for each pair of frames to produce estimates of the gain and bias variation behaviors as the true gain and bias were changing. The vectors were plotted over frame number to show the variation over time.

In the first round of simulation, the vector of gain estimates from the cross-array variation tracking algorithm was plotted against the true gain vector for 4 separate cases. The results from all four cases are shown in Figure 4.9. In the first case, the gain was constant, in the second case, the gain was linearly decreasing, in the third case, the gain was sinusoidal, and in the fourth case, the gain was constant with periodic dips.

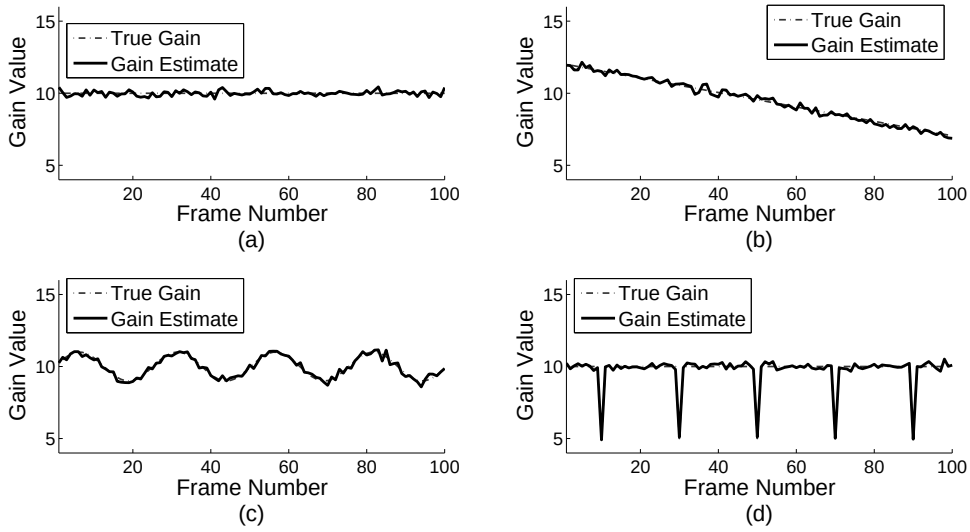

Figure 4.9: shows simulated gain variation estimates compared to the true gain in four different cases. The case in (a) is a constant gain value, (b) is a linearly decreasing situation, (c) has a sinusoidal gain, and (d) has a periodic dip in the gain.

In all four plots, the estimates show minor random variation while closely following the true trend of the gain values. The results indicate that a variation tracking analysis can be used to isolate gain variation effects that could be present in various data sources.

Furthermore, variation tracking analysis can be used to determine the source of some systematic effects. The periodic dip in the gain in Figure 4.9(d) is independent of variation in the bias and the algorithm can verify the independence.

To test the capability of the variation tracking to distinguish between trends in the gain and bias, the simulation was repeated for a periodic dip in the gain and a constant bias. The resultant estimates are shown in Figure 4.10(a) and (c). Then the simulation was reversed, with the gain being constant and the bias exhibiting a periodic dip. Those results are shown in Figure 4.10(b) and (d). In both sets of results, the estimates closely follow the real gain and bias trends including correctly identifying the source of the periodic dips. The two sets of results show that the variation tracking algorithm is capable of distinguishing between differences in the gain and bias trends.

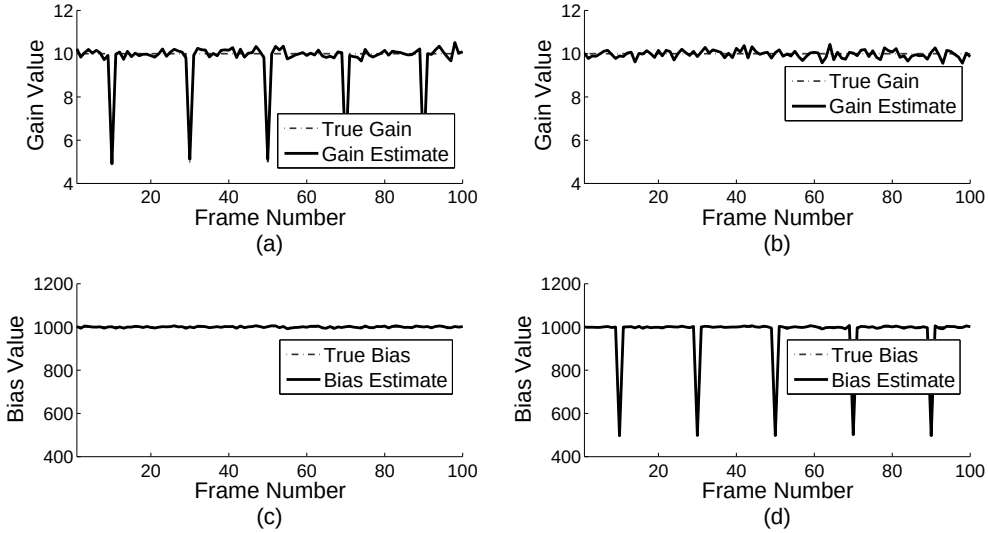

Figure 4.10: shows simulated gain and bias estimates compared to the true values in two separate cases. The case in (a) and (c) is one with the the gain having periodic dips and the bias is a constant value. The second case in (b) and (c) is the reverse where the gain is constant and the bias has periodic dips.

The gain trends in both data sets must be closely aligned. If they are not, the S3NUC equations will produce erroneous results due to the assumption that the global values are the same in the frame pair. A simulation was repeated in the same manner as described above with four different cases where the gain between the two sets of data are different. The estimates are shown in Figure 4.11 in a solid line along side the two true gain values in different dashed lines. In the first case, shown in Figure 4.11(a), both gains are constant but have different values. In the second, (b), and third, (c), cases, the gains are sinusoidal but have either a different amplitude or are out of phase respectively. In the fourth case in (d), the gains have a linear trend but the first set of data has an inverse trend to the gain in the second set.

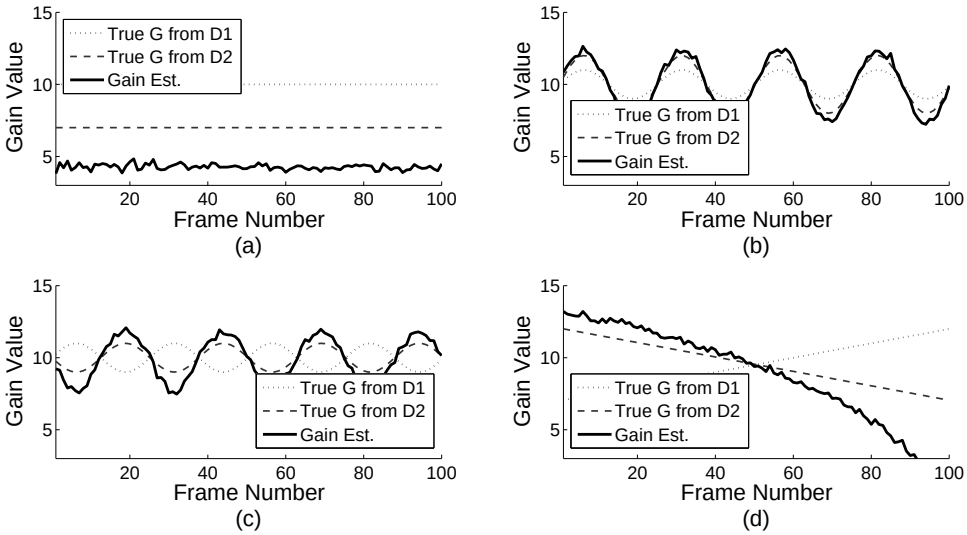

Figure 4.11: shows the gain estimates compared to the true value in four cases when the gain in the two data sets are not the same. The case in (a) is when the gain is constant but at two different values. The cases in (b) and (c) show a sinusoidal gain but at different amplitudes or different phases respectively. The case in (d) is where the gain is linearly increasing in one set of data and linearly decreasing at the same rate in the second.

All four sets of results in Figure 4.11 show that if there is a difference between the gains in the two data sets, the gain estimates from the variation tracking algorithm will not

be accurate. Each set shows that as the difference in the gains increases, the accuracy of the estimates decreases. In the fourth case in (d) with two opposing gain trends, as the simulation is allowed to continue, the gain estimates will approach zero and eventually become negative. While zero and negative gain estimates are erroneous results, they do indicate that there is a difference in the true gains between the two data sets.

While the gain estimates themselves are inaccurate for mismatched gain trends, in each case, the gain estimates are indicative of the gain trend in the data set with a higher mean photocount. The relationship between the estimates and gain from the more intense data set is especially apparent in the third and fourth set of results in Figure 4.11 seen in (c) and (d). The reason for the relationship comes from the derivation of Equation (3.49) where the subtractions are removing all variables except for the gain, G, and the mean photocount difference, $\Delta\bar{K}$, then dividing to solve for G. Because of the relationship between $\Delta\bar{K}$ and G, the gain trend is dependent on the more intense data set where $\Delta\bar{K}$ is present.

4.3.2 CMOS Camera Results.

To analyze the CMOS camera for variation, two smaller data sets of 1000 images each were used for analysis. The moments for the cross-array configuration were computed for each frame. From the moments, the gain and bias estimates were calculated using the S3NUC moment equations. The calculations were repeated over the set of a thousand frame pairs. The image size of 512×512 pixels ensured there were sufficient samples to achieve a precise estimate for all parameters. The gain and bias values were plotted over the frame number and the results are shown together in Figure 4.12 with the gain vector in (a) and the bias in (b).

The gain variation tracking shows that there significant global gain fluctuations in the first 500 frames of the CMOS data. After 500, the gain stabilizes at a value around 2×10^{-5} digital counts per photocount. There is some noise present on the trend but over all the estimates show a clear trend in the global gain values. The bias trend is much more

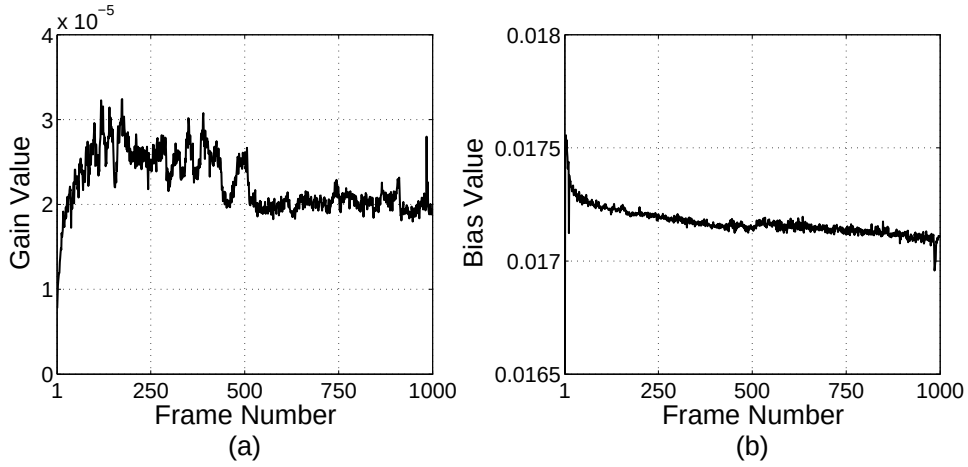

Figure 4.12: shows the estimated variation trends in CMOS data over time for the gain in (a) and bias in (b)

stable and shows a very clear, approximate linear decrease over time. Both the gain and bias trends are a result of the camera's active cooling achieving a steady-state temperature around frame 500.

4.3.3 CCD Camera Results.

Data collected from the CCD camera was analyzed for variation in the same method as the CMOS data. 1000 pairs of frames were collected and analyzed using the moment equations to produce vectors for the gain and bias over time. The frames were 640×480 pixels in size, ensuring an adequate sample size to produce precise estimates. The gain and bias vectors were plotted over frame number in Figure 4.13 with the gain vector in (a) and the bias in (b).

Neither the gain nor bias vectors show the same stable trend observed in the CMOS data from Figure 4.12. The gain vector slowly drops over time and then, at approximately frame 700, jumps back up in value. The bias exhibits a similar trend of falling values over time then a jump up in value at approximately frame 700. The variation in both the gain and bias are a result of the camera firmware compensating for thermal effects as this camera did not have active cooling like the CMOS camera. The variation tracking algorithm shows

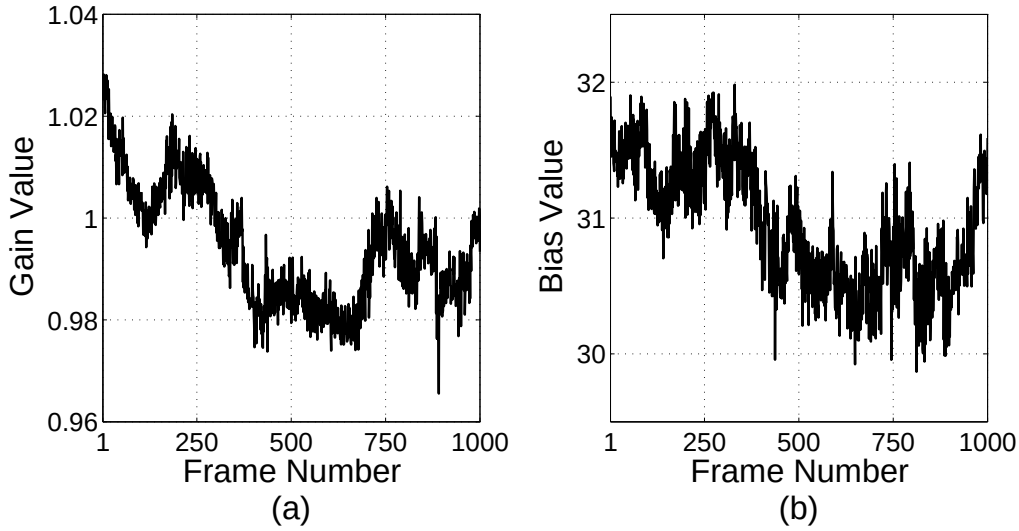

Figure 4.13: shows the estimated variation trends in CCD data over time for the gain in (a) and bias in (b)

that it can produce trends in the gain and bias that are indicative of compensation features in the cameras. But these trends may not be precisely accurate due to offsets in the gain and bias values between the two data sets as discussed in Section 4.3.1.

4.3.4 LADAR Results.

In the TigerEye Flash LADAR data sets, the primary parameter of concern was the average gain of the system over time, as the TigerEye system is known to have systematic, temporal gain variation. To collect two data sets of different intensities from the LADAR system, a filter was used on the laser aperture to attenuate the power output. To capture the change in power, a target was set up in the near-field range, approximately 10 meters from the camera aperture. The target needed to fill a majority of the Field of View (FOV) so that the data capture could collect the most returning laser light. If the target did not fill a large majority of the FOV, the background scene, with no returning laser light, would dominate the frame average. The average lack of returning laser light would result in a $\Delta\bar{K}$ value at or near zero and the variation tracking algorithm would not work.

Data sets were taken with and without the filter. Both data sets were read in, correctly shifted using the marker frames, and analyzed in the same method as the CMOS camera data. The first ten range gates, each with 20 frames, from the data were used providing 200 frames for analysis. The gain estimates showed a periodic trend which was expected based on performance from prior research [28]. To quantitatively compare the results, the gain estimate was compared to the response from a pixel that was not on the target. The off-target pixel observes a nearly constant photocount, but is affected by a varying gain trend. For a length of 200 frames, both the gain and off-target pixel vectors were normalized by their mean values and the error between the two was calculated. Figure 4.14 shows the normalized error plot over the 200 frames analyzed.

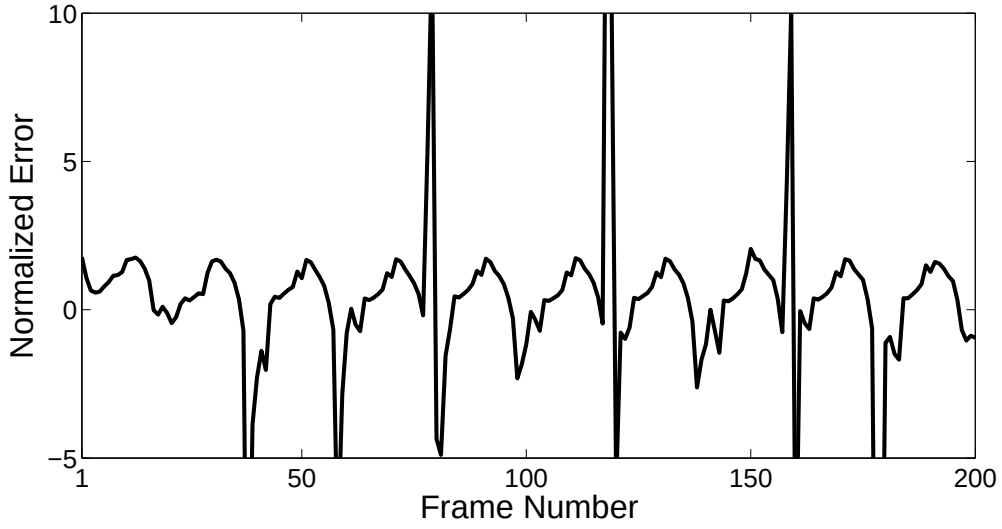

Figure 4.14: shows the error between the normalized off-target pixel's response and the gain trend estimat in LADAR Data from the ASC TigerEye system

Across the 200 frames analyzed, the majority of the error was between 0 and 2 normalized units and had a mean of 1.9589×10^{-15}. The magnitude of the error indicates that the gain trend matched the off-target pixel's response. There is some systematic noise still present in the error shown in Figure 4.14. The remaining systematic noise is not from

gain variation. Thus, the gain variations were accurately tracked by the off-target pixels and estimated by the variation tracking algorithm.

The primary benefit in extracting the gain variation trends in a LADAR system is that the variation affects the returning laser pulse shapes which can adversely reflect range calculations. By extracting the gain variation trend, it can be used to correct the data to provide more accurate ranging results.

V. Conclusion

The methods of estimation in S3NUC have been shown to provide accurate estimates of the fixed pattern noise, or systematic error, in photodetector FPAs. The S3NUC method uses statistical moments of a linear model with noise to exploit random error to correct systematic error in the output data. S3NUC can produce accurate results when observing a nonuniform source field, though performance does suffer slightly due to additional random noise being introduced. The analysis was applied to data collected with CMOS and CCD based cameras and a estimate of the fixed pattern was used to correct the output data to validate the algorithm.

S3NUC may also be used to track global variations in the gain and bias of the output data. The results show that the variation tracking implementation can achieve accurate results and can distinguish trends between different parameters when the trends are the same between the two data sets used. The estimation accuracy suffers when the gain and bias trends differ between the two data sets. Simulation proved that the estimate values became erroneous then there was a difference in the values between frame pairs. The same analysis was applied to data collected with the CMOS, CCD, and LADAR systems. The results obtained from the collected data show clear trends in the gain and bias. The trends in the LADAR system match predictions made from prior research in the area.

Based on the results obtained in the research contained, S3NUC provides a viable method for correcting fixed patterns from photodetector array. S3NUC provides this information without the need for perfectly uniform sources with known intensities that are required for traditional NUC methods that preserve radiometrically accurate results. Furthermore, the equations for S3NUC can be applied to accurately track global variations in systems that have variation issues. The combination of uses certifies the S3NUC method's usefulness in image processing applications.

5.1 Future Work

In the research conducted, the S3NUC equations were derived and tested for applicability. Future work would entail a more thorough testing of the algorithm to define the limits and requirements for accurate results. Due to the lack of the necessary lab equipment, the two-point NUC method was not tested with collected data to compare results to the S3NUC results. Further testing with collected data is necessary before implementation in a real-world environment.

During derivation, a method of using a fourth order moment, excess kurtosis, to eliminate the need for two data sets was analytically proven. However, testing in simulation proved that the excess kurtosis value over a finite set had such high variation that accurate gain and bias estimates were impossible to achieve without impractically large data sets. Future research could include further examination of how large of a data set would be required or if there is another use for the excess kurtosis equation.

Bibliography

[1] Bhatnagar, A., C. Debaes, H. Thienpont, and D. A. B. Miller. “Receiverless detection schemes for optical clock distribution”. volume 5359, 352–359. 2004.

[2] Cain, Stephen and Steven Johnson. “Bound on range precision for shot-noise limited ladar systems.” *Applied Optics*, 47(28):5147–54, 2008.

[3] Deas, Brian T. “Pulse shape correlation for laser detection and ranging (LADAR)”, 2010.

[4] Goodman, Joseph W. *Introduction to Fourier optics*. McGraw-Hill, San Francisco, 1968.

[5] Goodman, Joseph W. *Statistical optics*. Wiley, New York, 1985.

[6] Haight, Frank A. *Handbook of the Poisson distribution*. Wiley, New York, 1967.

[7] Hambley, Allan R. *Electrical Engineering : Principles and Applications*. Pearson Prentice Hall, Upper Saddle River, N.J., 4th edition, 2008.

[8] Hardie, R. C., M. M. Hayat, E. Armstrong, and B. Yasuda. “Scene-based nonuniformity correction with video sequences and registration”. *Applied Optics*, 39(8):1241–50, 2000.

[9] Harris, John G. “Continuous-time calibration of VLSI sensors for gain and offset variations”. *Smart Focal Plane Arrays and Focal Plane Array Testing*, volume 2474, 23. 1995.

[10] Harris, John G. and Yu-Ming Chiang. “Nonuniformity correction using the constant-statistics constraint: analog and digital implementations”. *Infrared Technology and Applications XXIII*, volume 3061, 895. 1997.

[11] Hayat, Majeed M., Sergio N. Torres, Ernest Armstrong, Stephen C. Cain, and Brian Yasuda. “Statistical Algorithm for Nonuniformity Correction in Focal-Plane Arrays”. *Applied Optics*, 38(5), 1999.

[12] Holst, Gerald C. *CCD arrays, cameras, and displays*. JCD Pub. ; SPIE Optical Engineering, Winter Park, FL; Bellingham, Wash., USA, 1998.

[13] Inc., Advanced Scientific Concepts. “Technology Overview”, 2013.

[14] Itzler, Mark A., Xudong Jiang, Rafael Ben-Michael, Bruce Nyman, and Krystyna Slomkowski. “Single photon avalanche photodiodes for near-infrared photon counting”. volume 6900, 69001E. 2008.

[15] Jordan, S., M. Gebhardt, E. Armstrong, H. Larsson, and O. Steinvall. "Scene-based algorithm for range/intensity estimation correction for the FLASH 3D LADAR system". *Proc SPIE Int Soc Opt Eng Proceedings of SPIE - The International Society for Optical Engineering*, 7684, 2010.

[16] Jordan, S. P. "Range Estimation Algorithm Comparison in 3-D Flash LADAR Data", 01/01 2009.

[17] Milton, A. F., F. R. Barone, and M. R. Kruer. "Influence Of Nonuniformity On Infrared Focal Plane Array Performance". *Optical Engineering*, 24(5):245855, 1985.

[18] Narendra, P. M. and N. A. Foss. "Shutterless Fixed Pattern Noise Correction For Infrared Imaging Arrays". *SPIE: Technical Issues in Focal Plane Development*, volume 282, 44–51. The International Society for Optical Engineering, 1981.

[19] Patel, Jagdish K. and Campbell B. Read. *Handbook of the Normal Distribution*. CRC Press, 2nd edition, 1996.

[20] Pebay, Philippe. *Formulas for Robust, One-Pass Parallel Computation of Covariances and Arbitrary-Order Statistical Moments*. Technical Report SAND2008-6212, Sandia National Labs, 2008.

[21] Perry, David L. and Eustace L. Dereniak. "Linear theory of nonuniformity correction in infrared staring sensors". *Optical Engineering*, 32(8):1854, 1993.

[22] Richmond, Richard D. and Stephen C. Cain. *Direct-detection LADAR systems*. 2010.

[23] Sakoglu, Unal, Russell C. Hardie, Majeed M. Hayat, Bradley M. Ratliff, and J. Scott Tyo. "An algebraic restoration method for estimating fixed-pattern noise in infrared imagery from a video sequence". volume 5558, 69–79. 2004.

[24] Schulz, Max J. and Larry V. Caldwell. "Nonuniformity correction and correctability of infrared focal plane arrays". *Infrared Imaging Systems: Design, Analysis, Modeling, and Testing VI*, volume 2470, 200. 1995.

[25] Scribner, D. A., M. R. Kruer, J. C. Gridley, and K. Sarkady. "Physical Limitations To Nonuniformity Correction In IR Focal Plane Arrays". *Focal Plane Arrays: Technology and Applications*, volume 0865, 185. 1988.

[26] Scribner, Dean A., Kenneth A. Sarkady, John T. Caulfield, Melvin R. Kruer, G. Katz, C. J. Gridley, and Charles Herman. "Nonuniformity correction for staring IR focal plane arrays using scene-based techniques". *Infrared Detectors and Focal Plane Arrays*, volume 1308, 224. 1990.

[27] Scribner, Dean A., Kenneth A. Sarkady, Melvin R. Kruer, John T. Caulfield, J. D. Hunt, and Charles Herman. "Adaptive nonuniformity correction for IR focal-plane arrays using neural networks". *Infrared Sensors: Detectors, Electronics, and Signal Processing*, volume 1541, 100. 1991.

[28] Seal, Michael D. "Nonlinear Time-Variant Response in an Avalanche Photodiode Array Based Laser Detection and Ranging System", 2007.

[29] Sedra, Adel S. and Kenneth C. Smith. *Microelectronic Circuits*. Oxford University Press, Inc., New York, 5th edition, 2004.

[30] Stettner, Roger, Howard Bailey, and Steven Silverman. *Three dimensional Flash LADAR focal planes and time dependent imaging*. Technical report, Advanced Scientific Concepts, 2006.

[31] Streetman, Ben G. and Sanjay Banerjee. *Solid State Electronic Devices*. PrenticeHall, Upper Saddle River, New Jersey, 5th edition, 2000.

[32] Tektronix. "Understanding and Characterizing Timing Jitter", 2012. http://info.tek.com/rs/tektronix/images/55W_16146_5_MR_Letter.pdf.

[33] Terriberry, Timothy B. "Computing Higher-Order Moments Online", 2008. http://people.xiph.org/~tterribe/notes/homs.html.

REPORT DOCUMENTATION PAGE

Form Approved
OMB No. 0704–0188

1. REPORT DATE *(DD–MM–YYYY)*	2. REPORT TYPE	3. DATES COVERED *(From — To)*
26–03–2015	Master's Thesis	Oct 2014–Mar 2015

4. TITLE AND SUBTITLE

Static Scene Statistical Non-Uniformity Correction

5a. CONTRACT NUMBER

5b. GRANT NUMBER

5c. PROGRAM ELEMENT NUMBER

6. AUTHOR(S)

Catarius, Adrian M., First Lieutenant, USAF

5d. PROJECT NUMBER

5e. TASK NUMBER

5f. WORK UNIT NUMBER

7. PERFORMING ORGANIZATION NAME(S) AND ADDRESS(ES)

Air Force Institute of Technology
Graduate School of Engineering and Management (AFIT/EN)
2950 Hobson Way
WPAFB, OH 45433-7765

8. PERFORMING ORGANIZATION REPORT NUMBER

AFIT-ENG-MS-15-M-062

9. SPONSORING / MONITORING AGENCY NAME(S) AND ADDRESS(ES)

Intentionally Left Blank

10. SPONSOR/MONITOR'S ACRONYM(S)

11. SPONSOR/MONITOR'S REPORT NUMBER(S)

12. DISTRIBUTION / AVAILABILITY STATEMENT

DISTRIBUTION STATEMENT A:
APPROVED FOR PUBLIC RELEASE; DISTRIBUTION UNLIMITED

13. SUPPLEMENTARY NOTES

14. ABSTRACT

Non-Uniformity Correction (NUC) is required to normalize imaging detector Focal-Plane Array (FPA) outputs due to differences in the end-to-end photoelectric responses between pixels. Currently, multi-point NUC methods require static, uniform target scenes of a known intensity for calibration. Conversely, scene-based NUC methods do not require a priori knowledge of the target but the target scene must be dynamic. The new Static Scene Statistical Non-Uniformity Correction (S3NUC) algorithm was developed to address an application gap left by current NUC methods. S3NUC requires the use of two data sets of a static scene at different mean intensities but does not require a priori knowledge of the target. The S3NUC algorithm exploits the random noise in output data utilizing higher order statistical moments to extract and correct fixed pattern, systematic errors. The algorithm was tested in simulation and with measured data and the results indicate that the S3NUC algorithm is an accurate method of applying NUC. The algorithm was also able to track global array response changes over time in simulated and measured data. The results show that the variation tracking algorithm can be used to predict global changes in systems with known variation issues.

15. SUBJECT TERMS

focal-plane arrays, nonuniformity correction, fixed-pattern noise, laser detection and ranging, skewness

16. SECURITY CLASSIFICATION OF:			17. LIMITATION OF ABSTRACT	18. NUMBER OF PAGES	19a. NAME OF RESPONSIBLE PERSON
a. REPORT	b. ABSTRACT	c. THIS PAGE			Maj Michael D. Seal, PhD (ENG)
U	U	U	UU	61	19b. TELEPHONE NUMBER *(include area code)* (937) 255-3636 x3369 Michael.Seal@afit.edu